

Multidimensional Modelling of Cross-Beam Energy Transfer for Direct-Drive Inertial Confinement Fusion

(Hopefully soon to be Dr.) Philip W. X. Moloney

IMPERIAL

June 2024

Submitted in partial fulfilment of the requirements for the degree of
Doctor of Philosophy of Imperial College London

Department of Physics
Imperial College London
Prince Consort Road
London SW7 2AZ

List of Acronyms

Rad-MHD Radiative-Magnetohydrodynamics

MHD Magnetohydrodynamics

LPIs Laser-Plasma Instabilities

CBET Cross-Beam Energy Transfer

ICF Inertial Confinement Fusion

IAW Ion Acoustic Wave

NIF National Ignition Facility

1 Simulations of Cross-Beam Energy Transfer for Magnetised Direct-Drive

This chapter describes a set of simulations which were conducted to understand the role of Cross-Beam Energy Transfer (CBET) in magnetised, direct-drive implosions. Magnetised Inertial Confinement Fusion (ICF) is a promising route to achieving higher target gains, due to the reduction of thermal energy loss at stagnation and additional confinement of the alpha particles responsible for burn propagation. For direct-drive implosions, magnetisation can significantly alter the coronal plasma profiles, due to the introduced anisotropy of thermal transport. The Ion Acoustic Wave (IAW) dispersion relation, which mediates CBET interactions, depends upon the background plasma and therefore significantly altered temperature and density profiles could alter the action of CBET. Before the development of SOLAS, no direct-drive suitable CBET model existed, which was integrated into a Radiative-Magnetohydrodynamics (Rad-MHD) code. Therefore, the CHIMERA-SOLAS computational model has allowed the effect of magnetisation on CBET to be studied for a direct-drive implosion.

The chapter begins with a review of experimental and computational work on magnetised ICF, with a particular focus on magnetised direct-drive. Work presented in this chapter focuses on the study of *exploding-pusher* experiments. These are very different implosions to the typical *central hot-spot* ignition designs, presented in previous chapters, so a short summary of exploding pushers is also provided. Simulation results are presented of 1-D and 2-D, unmagnetised exploding pushers, both with and without the effect of CBET, which demonstrate that CBET does significantly alter the implosion. This is followed by an investigation of how various extended-Magnetohydrodynamics (MHD) terms affect the implosion, including the Nernst effect, the Lorentz force and resistive diffusion of the magnetic field. Results are given of how magnetisation affects the CBET interaction and ultimately how it changes the stagnation shape of the target. The results presented, demonstrate that redistribution of deposited power due to CBET, reduced the amplitude of the stagnation asymmetry, which originated from the polar beam configuration used, due to the presence of a field coil at the equator. However, the reduction of asymmetry was consistent for different initial seed magnetic field values, and therefore CBET was not observed to be sufficiently strongly affected by magnetisation, to lead to observable signatures in experimental measurements. The chapter concludes with a summary of the work and suggestions of additional experimental configurations, which may leave a more significant signature of magnetisation altering CBET.

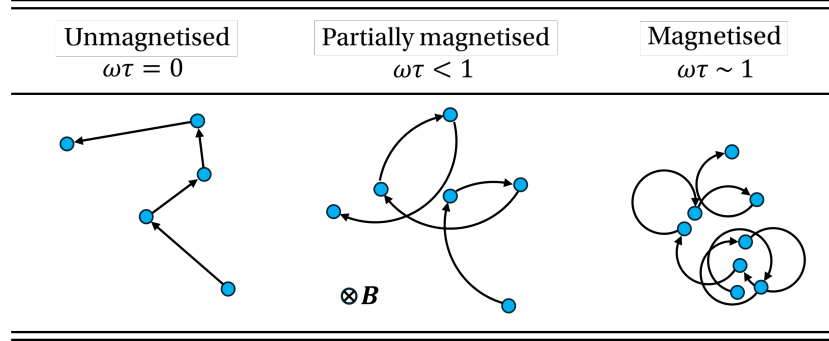


Figure 1.1: Cartoon to illustrate the effect of magnetisation on collisions, and therefore transport, of a test positive charge. As the Hall parameter of the particle increases, diffusion is increasingly limited, and therefore collision transport is reduced.

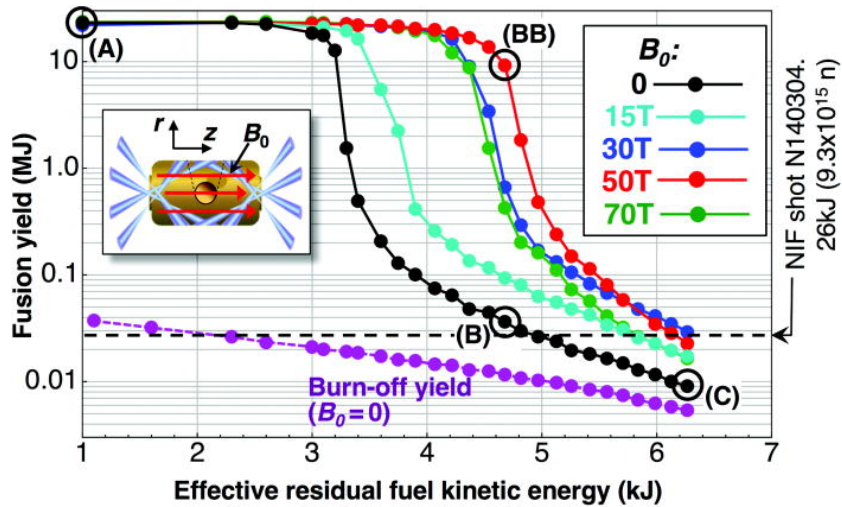


Figure 1.2: Simulated fusion yields versus effective residual fuel kinetic energy under imposed low-mode radiation flux perturbations for imposed fields in the range $B_0 = 0 \rightarrow 70$ (T). The plot demonstrates with increasing departure from ideal compression (moving to the right on the x axis), magnetisation can enable the onset of the ignition. Reused with permission from Ref. [1].

1.1 Magnetised Inertial Confinement Fusion and Exploding Pushers

This chapter begins with a review of published work that is relevant to the simulations which are presented. Firstly, a short review of magnetised-ICF is presented which reviews both the key concepts, existing studies and potential challenges of the design. Both work on direct- and indirect drive is summarised, alongside recent theoretical progress on understanding how magnetisation can effect Laser-Plasma Instabilities (LPIs). The exploding pusher concept is then briefly explored to aid understanding of the implosion physics, which is markedly different to conventional hot-spot ICF.

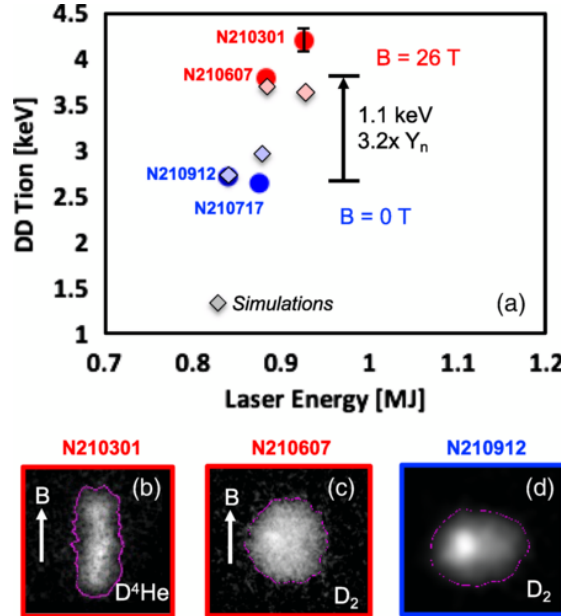


Figure 1.3: a) A 1.1 keV T_i increase was achieved by adding a 26 T B_0 field to a D2 gas capsule implosion on the National Ignition Facility (NIF). Also shown in the plot are the simulation results. b)–d) Equatorial shapes of the implosions. Reused with permission from Ref. [2].

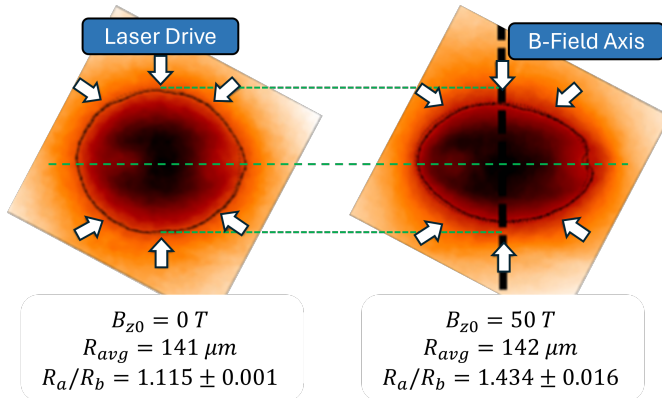


Figure 1.4: X-ray self emission images of (left) an unmagnetised and (right) a magnetised implosion. The average radius of the marked contour (corresponding to 40% of peak intensity), and the oblateness parameter R_a/R_b (ratio of major-to-minor axis) are listed below each image. The polar laser-drive is indicated by the white arrows, and the axis of the initial magnetic field by the black dashed line on the right. Applying an initial magnetic field demonstrated increased oblateness of the implosion. Adapted with permission from Ref. [3].

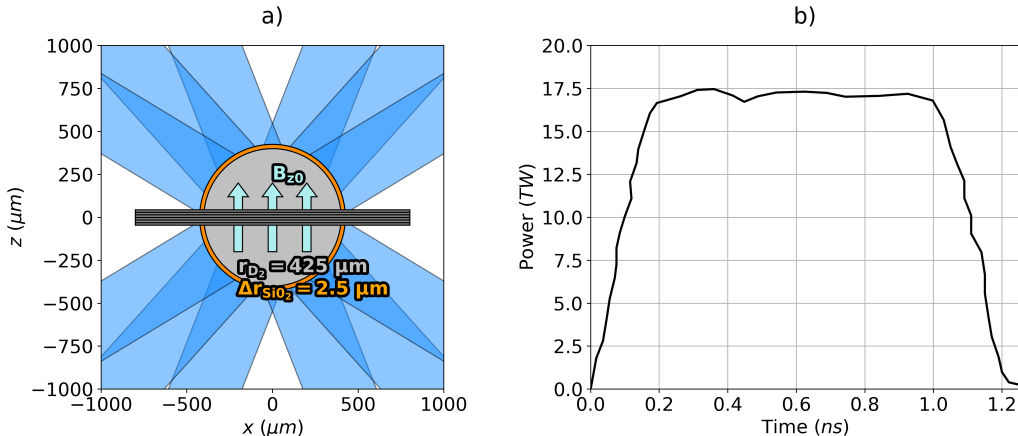


Figure 1.5: The initial conditions used for all simulations presented in this chapter. Panel a) plots the D₂ filled, glass shell capsule and direction of the initial magnetic field. An example field coil (illustrative and not included in simulations) is also shown, the presence of which necessitated the polar laser drive in experiments. Panel b) plots the laser pulse shape used, which had a total of 17.7 kJ laser energy.

1.1.1 Potential Benefits of Magnetisation

1.1.2 Existing Studies of Magnetised-ICF

1.1.3 Magnetised Laser-Plasma Instabilities

1.1.4 The Exploding-Pusher Configuration

1.2 Effect of Cross-Beam Energy Transfer in Unmagnetised Exploding Pushers

This section presents simulation results of the effect of CBET in exploding pushers on OMEGA. Both 1-D and 2-D CHIMERA-SOLAS simulations of 40-beam, polar driven exploding pusher experiments are presented, with a focus on how CBET acts to change the implosion. The 1-D results demonstrate that CBET significantly reduces the coupled laser energy to the implosion from ... to Simulations conducted in 2-D, with a full 3-D raytrace and CBET model, show that CBET alters spatial profile of the laser deposition, reducing asymmetry in the drive.

1.2.1 Simulation Configuration

1.2.2 1-D Simulations

1.2.3 2-D Simulations

1.3 The Effect of Magnetisation on Exploding-Pusher Implosions

This section presents results of a study of the effect that extended-MHD has on the 2-D exploding pusher simulations. Simulations were conducted with varying initial magnetic field

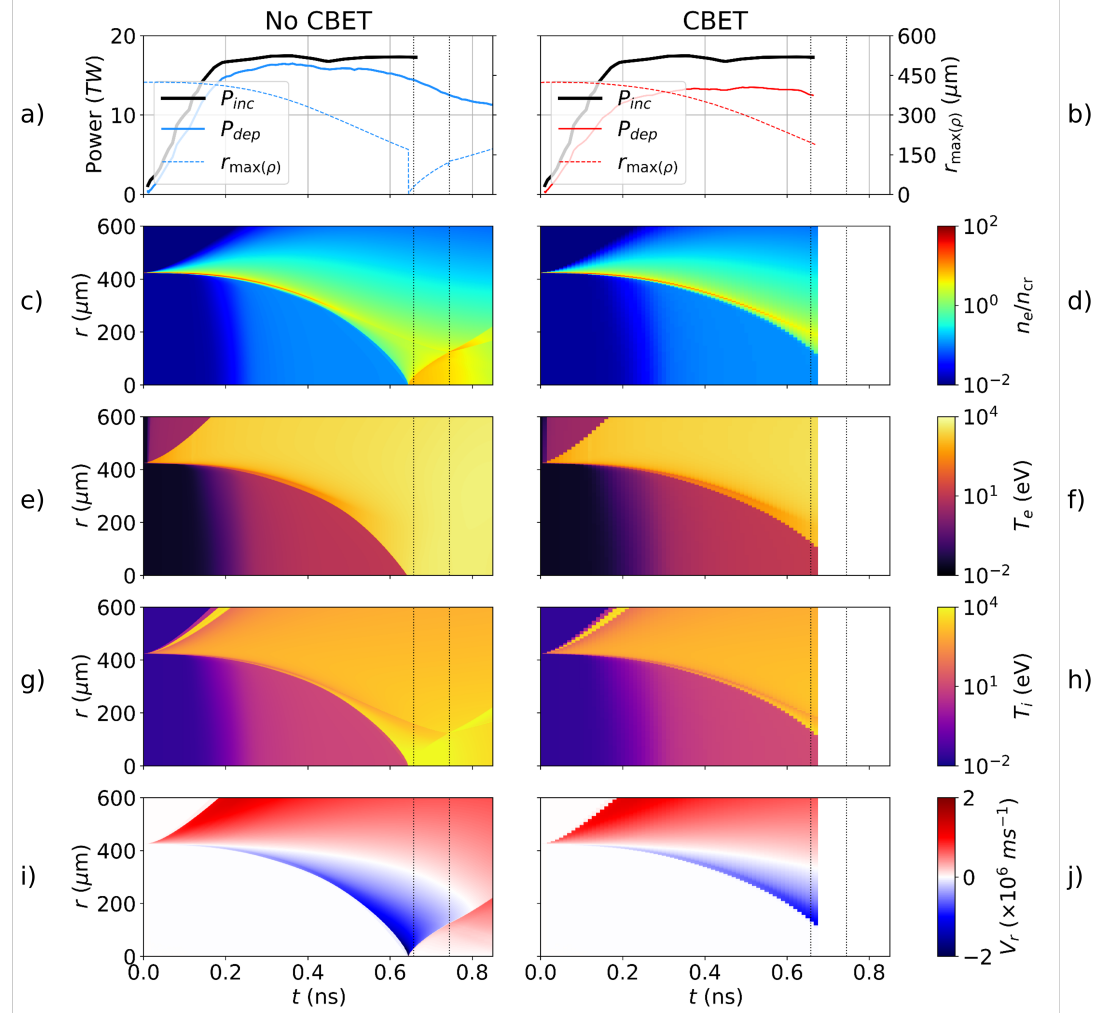


Figure 1.6: 1-D Simulation results both without (left) and with (right) CBET. The top row plots the incident and absorbed energy from the simulation on the left axis and the radius of maximum density on the right. In order, the next rows plot n_e , T_e , T_i and V_r . The full-width half-maximum times of the D2 yield are plotted as dotted vertical black lines on all panels.

strengths and particular terms turned off and on to deduce what the important physical processes are. Magnetised transport is important for both initial seed magnetic field implosions, resulting in large coronal Hall parameters and therefore significant anisotropy of the implosions. The results demonstrate that (resistive diffusion and the Lorentz force have very little impact on the implosion physics, due to the bulk of the plasma being highly resistive and high- β respectively)?????????????????????. The Nernst advection of magnetic field ??????????????????????

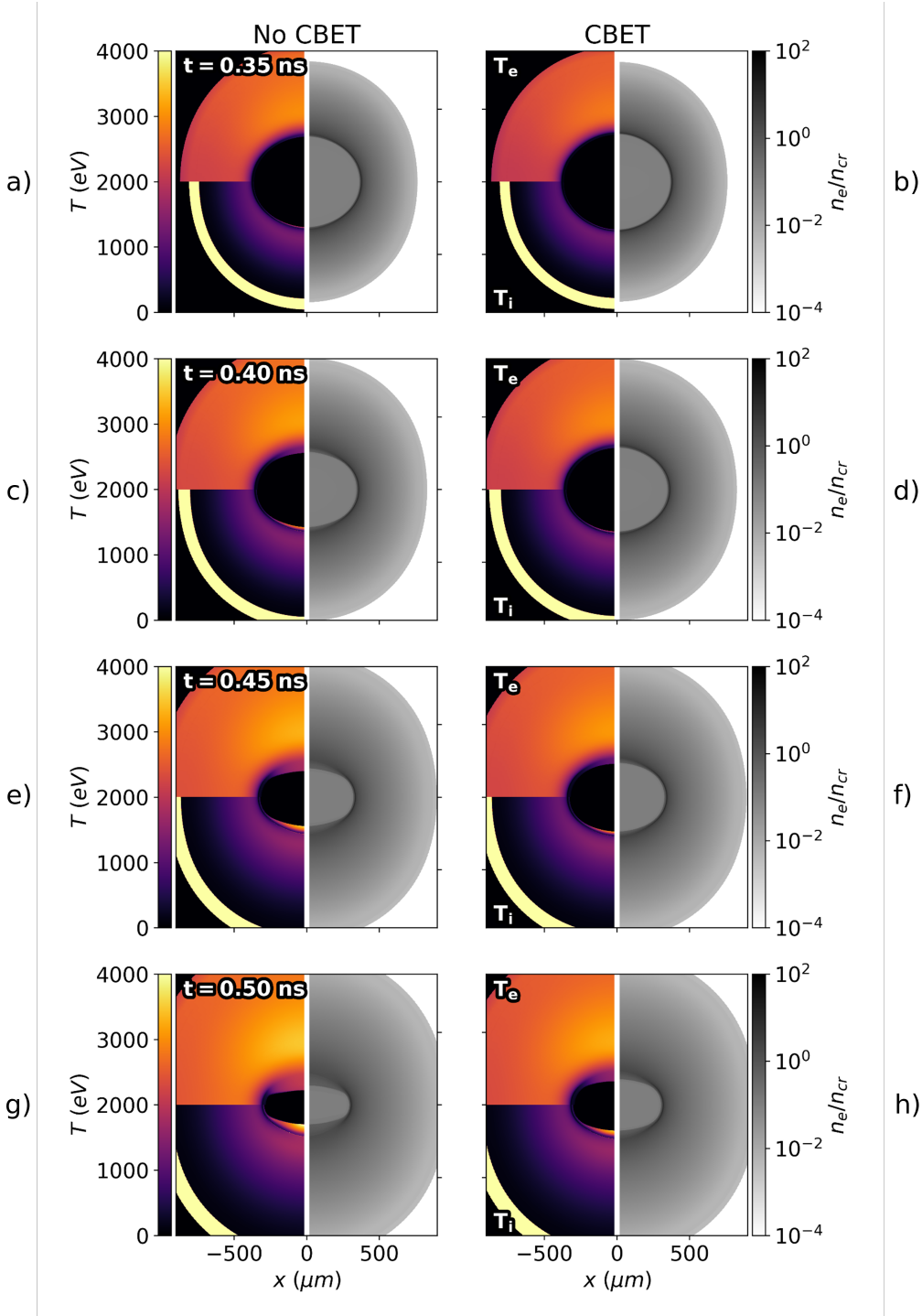


Figure 1.7: n_e (right-side), T_e (top-left-side) and T_i (bottom-left-side) plots from the 2-D, 0 $t_{text}T$ simulations without (left) and with (right) CBET at a variety of in-flight times. The decreased deposited energy due to CBET, results in lower coronal electron temperatures and therefore a slower, weaker shock being driven, which is especially evident at later times.

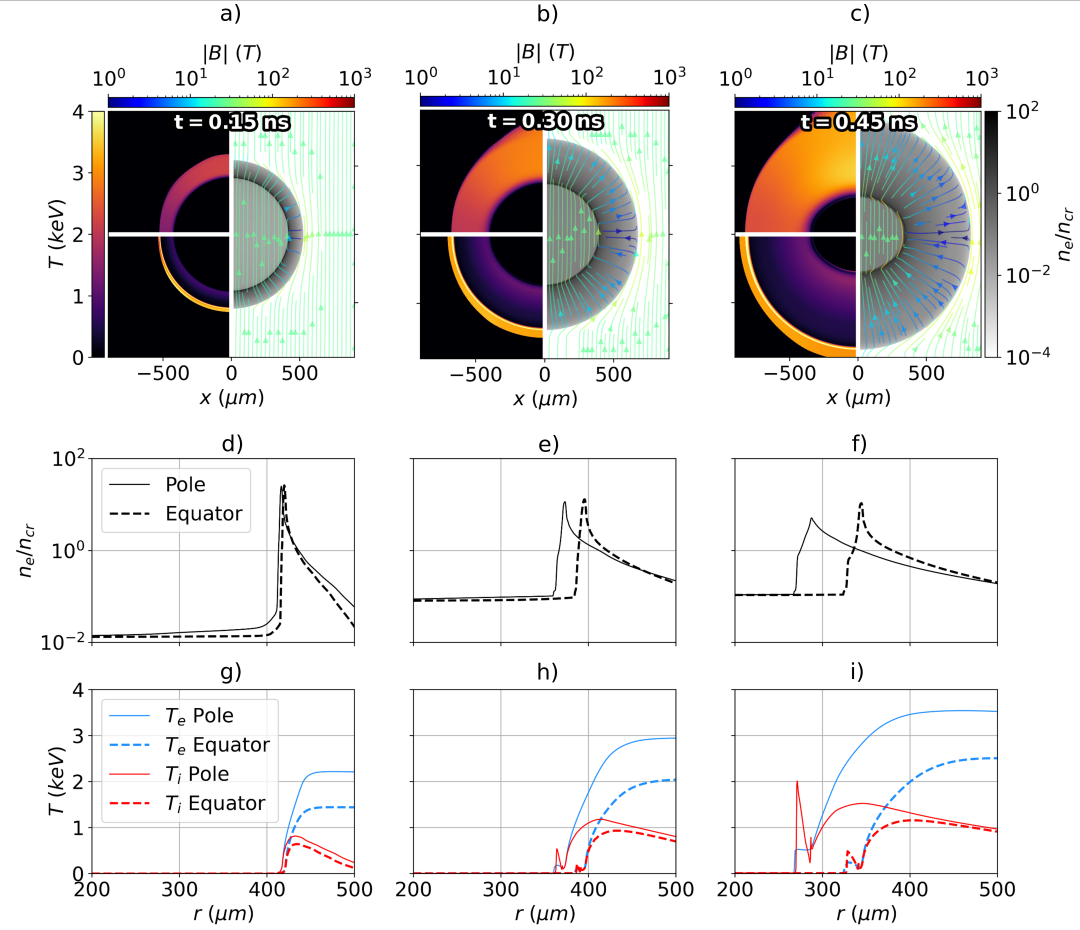


Figure 1.8: The development of the hydrodynamic variables and magnetic field structure from the $B_{z0} = 25$ T, CBET simulation. Panels a), b) and c) plot T_e (top-left), T_i (bottom-left), n_e (right) and \mathbf{B} (streamlines) at $t = 0.15, 0.30$ and 0.45 ns respectively. The approximately radially outward flowing, hot (and therefore highly conductive) ablating plasma pulls the magnetic field with it, resulting in radial \mathbf{B} field lines, which are weaker at the capsule equator. The radial field lines in the corona prevent angular equilibration of temperature, so act to keep heat at the poles. Compression of the SiO_2 shell leads to a non-radial field pile up on the inside edge of the maximum density, which is most clearly visible in panel c). Panels d), e) and f) plot n_e lineouts along the pole ($\theta = 0^\circ$) and equator ($\theta = 90^\circ$). Panels g), h) and i) plot equivalent T_e and T_i lineouts. These all show that the increased polar temperatures, partially due to beam geometry and partially due to magnetisation, lead to preferential ablation at the pole.

1.3.1 In-Flight Field Structure

1.3.2 Anisotropic Thermal Conduction

1.3.3 The Nernst Effect

1.3.4 Resistive Diffusion and the Lorentz Force

1.4 The Effect of Magnetisation on Cross-Beam Energy Transfer and Stagnation

This section presents results on how the magnetisation of the corona affects both CBET scattering and the stagnation shape of the implosion. As was shown in the previous sec-

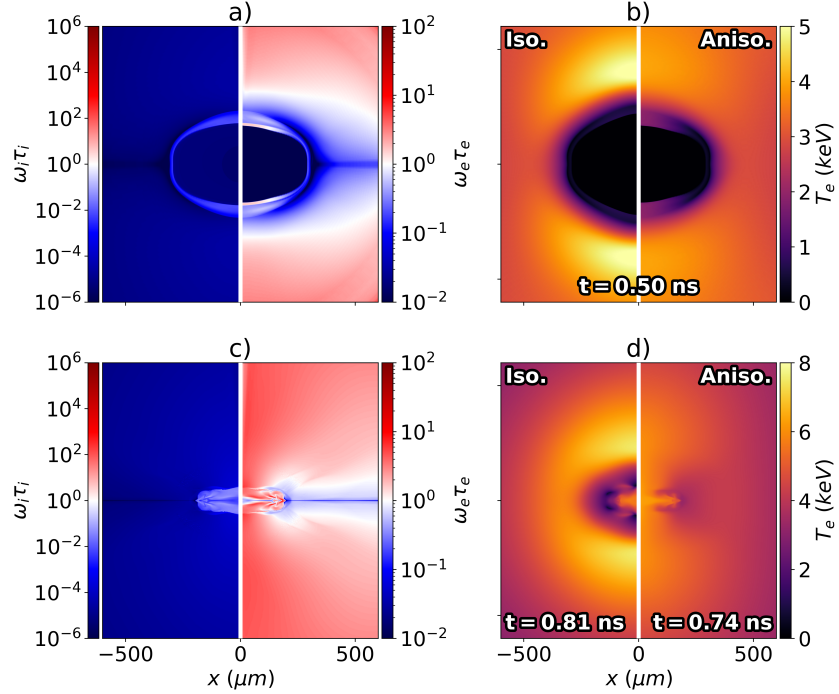


Figure 1.9: In-flight a) and bangtime c) Hall parameters, from the $B_{z0} = 25 \text{ T}$, no-CBET, anisotropic conduction simulation. Panel b) plots the T_e from the isotropically magnetised simulation (left-side) and anisotropic conduction simulation (right-side) in-flight. Panel c) plots the T_e from the isotropically magnetised simulation (left-side) and anisotropic conduction simulation (right-side) at peak neutron production. The electron Hall parameter is > 1 at the poles due to high magnetic fields and temperatures, leading to significantly restricted thermal conduction from magnetised transport at the poles. Isotropically magnetised conduction (*i.e.* setting $\kappa_{\parallel} = \kappa_{\perp}$), therefore results in a markedly different implosion morphology, as is shown in panels b) and d). Ion hall parameters peak at bangtime, with values reaching about $\omega_i \tau_i \sim 0.1$.

tions, the laser geometry leads to a significant mode $\ell = 2$ in the coronal plasma conditions, which is significantly amplified by anisotropic thermal conduction when magnetised. This long-wavelength perturbation is slightly reduced by CBET, consistent with existing literature on how CBET mitigates $\ell = 1$ asymmetries [4]. ‘No-CBET’ simulations were conducted, for which the coupled energy was kept the same as the equivalent CBET simulation, *i.e.* so CBET only acted to redistribute the deposited power, rather than reduce its magnitude. These results showed that the increasingly anisotropic coronal plasma profiles for increasing seed magnetic field strengths did lead to changes in the CBET scattering, this was too small an effect to lead to experimentally observable changes in behaviour.

Table 1.1: Results of all Simulations. In the CBET column, ‘~’ indicates CBET affecting the magnitude, but *not* spatial location, of deposition.

Run	Dim.	CBET	Note	B_{z0} (T)	t_b (ns)	$\langle T_i \rangle$ (keV)	Y_n ($\times 10^{10}$)	Δ_b (ps)	R_2/R_1
1	1-D	Off	-	0	0.69	14.66	11.62	87	$1.00^{+0.00}_{-0.00}$
2	1-D	On	-	0					$1.00^{+0.00}_{-0.00}$
3	2-D	Off	-	0	0.71	8.44	6.20	148	$2.96^{+0.20}_{-0.19}$
4	2-D	~	-	0	0.75	7.61	5.23	153	$3.26^{+0.25}_{-0.23}$
5	2-D	On	-	0	0.75	7.77	5.46	148	$3.23^{+0.25}_{-0.23}$
6	2-D	Off	-	25	0.74	7.26	4.73	130	$3.80^{+0.41}_{-0.33}$
7	2-D	~	-	25	0.78	6.58	4.14	125	$4.55^{+0.50}_{-0.43}$
8	2-D	On	-	25	0.78	6.72	4.44	123	$4.32^{+0.47}_{-0.41}$
9	2-D	Off	-	50	0.73	6.82	3.73	134	$4.40^{+0.43}_{-0.38}$
10	2-D	~	-	50	0.78	6.30	3.30	130	$4.92^{+0.56}_{-0.48}$
11	2-D	On	-	50	0.78	6.37	3.52	129	$4.79^{+0.55}_{-0.47}$
12	2-D	Off	No Aniso.	25	0.81	6.40	5.02	118	$3.14^{+0.68}_{-0.50}$
13	2-D	Off	No Lor.	25	0.74	7.29	4.77	131	$3.80^{+0.41}_{-0.33}$
14	2-D	Off	No Nern.	25	0.73	7.41	4.85	130	$3.74^{+0.38}_{-0.32}$
15	2-D	Off	No Resis.	25	0.73	7.07	4.59	132	$3.84^{+0.42}_{-0.33}$

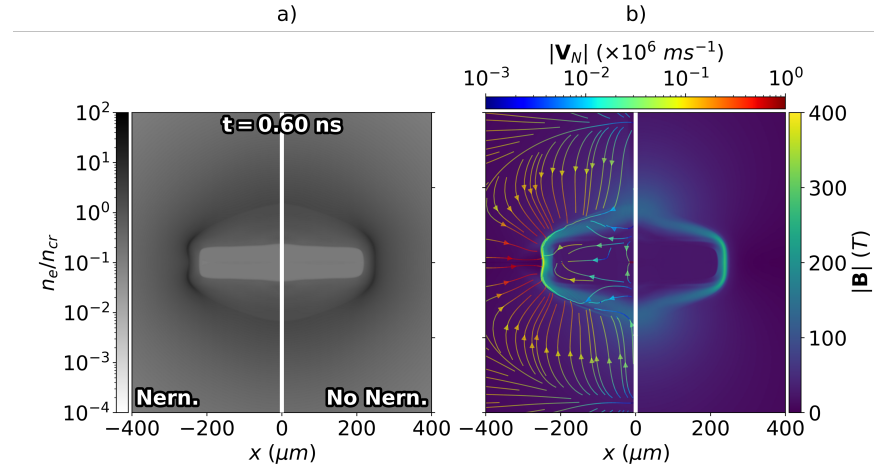


Figure 1.10: Panel a) plots in-flight electron density profiles from the $B_{z0} = 25$ T, no-CBET simulations with (left-side) and without (right-side) Nernst advection of the magnetic field. Panel b) plots magnetic field magnitude from the Nernst (left-side) and no-Nernst (right-side) simulation. The Nernst advection velocity is also plotted for the Nernst simulation as streamlines, coloured by speed. Advection of the field is important in the low Hall parameter equatorial region, pulling \mathbf{B} down ∇T_e , into the dense wall. Altered field at the equator impacts on the magnetised thermal conduction, which ultimately imprints on the density, as is seen in panel a).

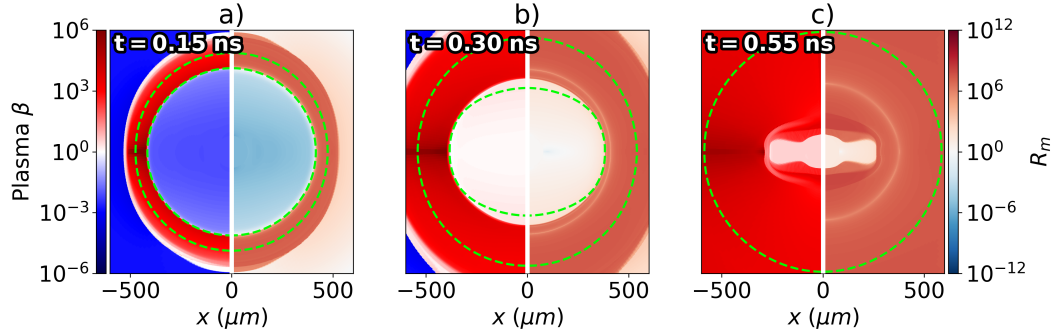


Figure 1.11: lol.

1.4.1 Analysis and Key Definitions

1.4.2 Spatial Change of CBET and Deposition from Magnetisation

1.4.3 Stagnation Profiles

1.5 Conclusions

1.5.1 Summary of Work

1.5.2 Future Work

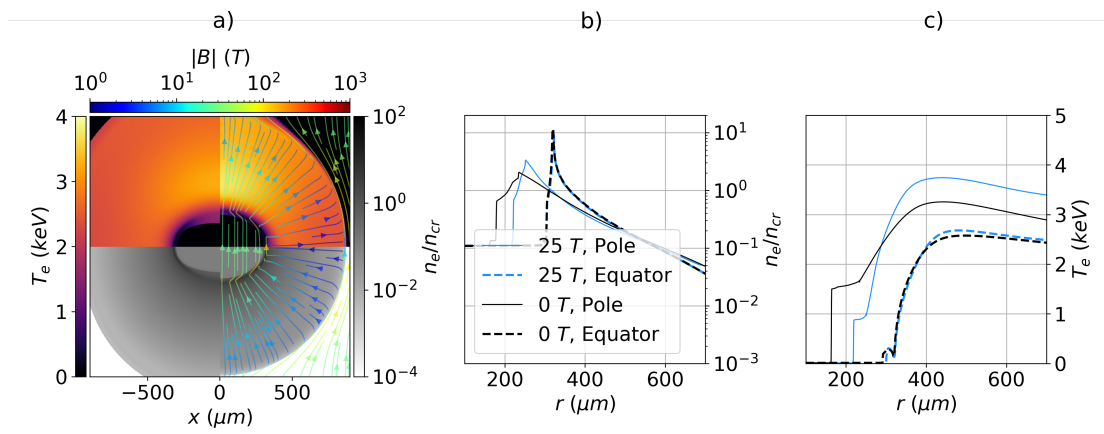


Figure 1.12: lol.

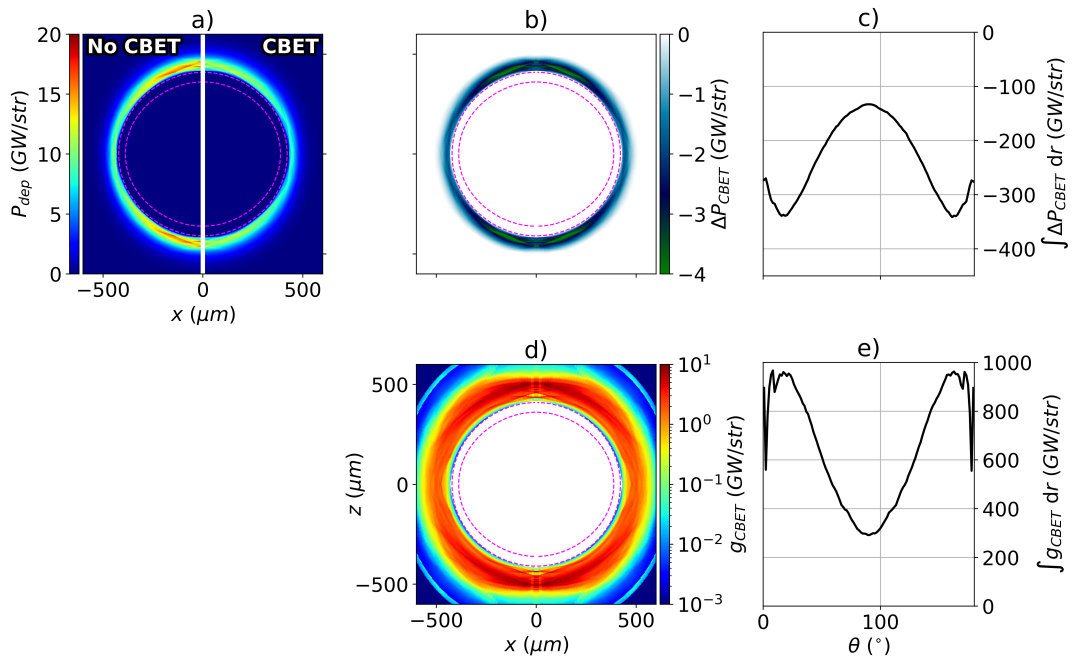


Figure 1.13: lol.

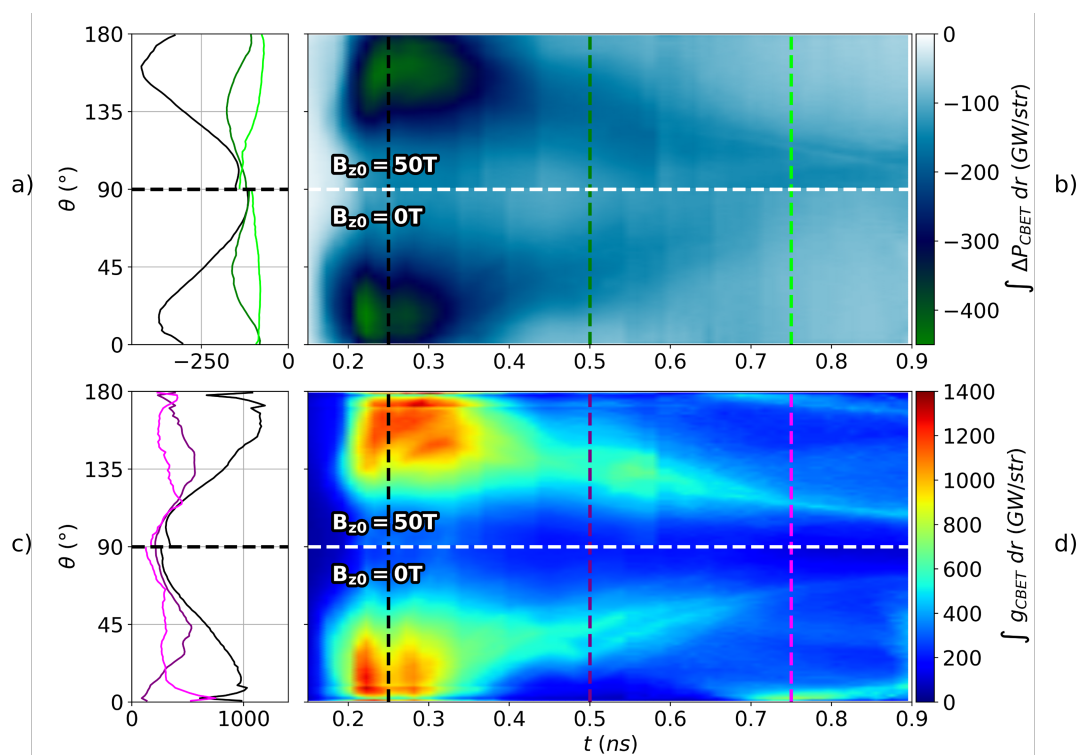


Figure 1.14: lol.

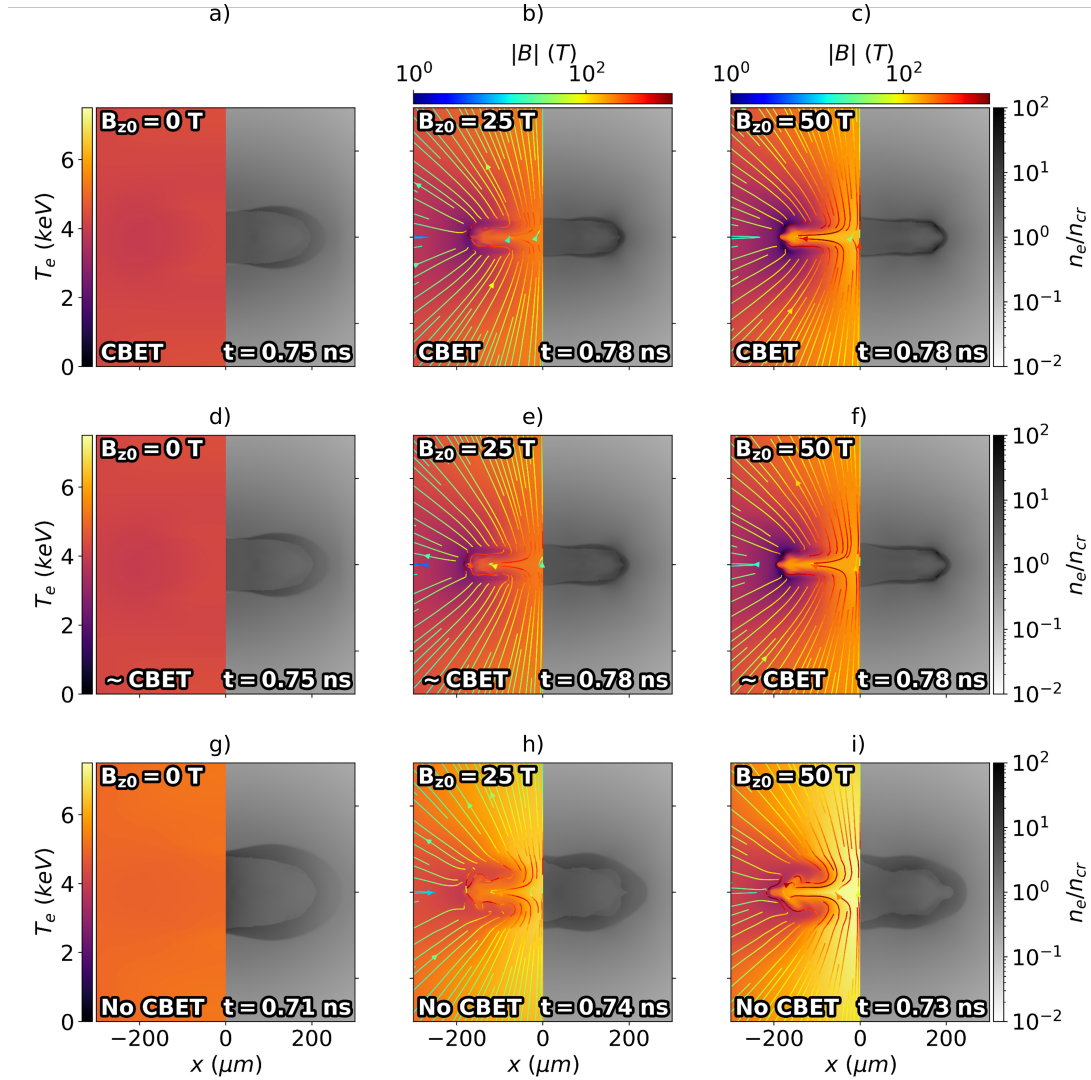


Figure 1.15: lol.

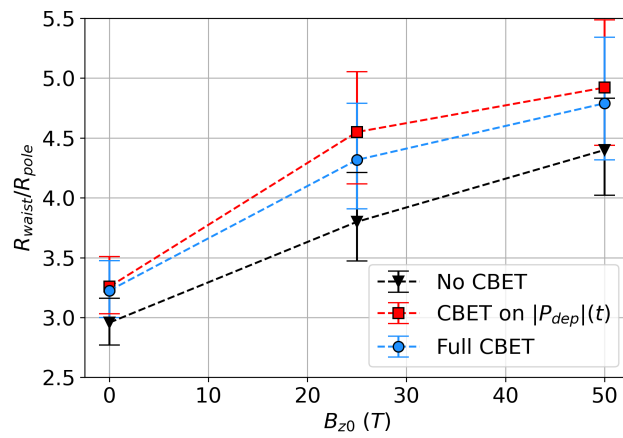


Figure 1.16: lol.

Appendices

Bibliography

- [1] L. J. Perkins, D. D.-M Ho, B. G. Logan, G. B. Zimmerman, M. A. Rhodes, D. J. Strozzi, D. T. Blackfield, and S. A. Hawkins. The potential of imposed magnetic fields for enhancing ignition probability and fusion energy yield in indirect-drive inertial confinement fusion. *Physics of Plasmas*, 24(6):062708, June 2017. ISSN 1070-664X, 1089-7674. doi: 10.1063/1.4985150. URL <https://pubs.aip.org/pop/article/24/6/062708/108192/The-potential-of-imposed-magnetic-fields-for>. 6
- [2] J. D. Moody, B. B. Pollock, H. Sio, D. J. Strozzi, D. D.-M. Ho, C. A. Walsh, G. E. Kemp, B. Lahmann, S. O. Kucheyev, B. Kozioziemski, E. G. Carroll, J. Kroll, D. K. Yanagisawa, J. Angus, B. Bachmann, S. D. Bhandarkar, J. D. Bude, L. Divol, B. Ferguson, J. Fry, L. Hagler, E. Hartouni, M. C. Herrmann, W. Hsing, D. M. Holunga, N. Izumi, J. Javedani, A. Johnson, S. Khan, D. Kalantar, T. Kohut, B. G. Logan, N. Masters, A. Nikroo, N. Orsi, K. Piston, C. Provencher, A. Rowe, J. Sater, K. Skulina, W. A. Stygar, V. Tang, S. E. Winters, G. Zimmerman, P. Adrian, J. P. Chittenden, B. Appelbe, A. Boxall, A. Crilly, S. O'Neill, J. Davies, J. Peebles, and S. Fujioka. Increased Ion Temperature and Neutron Yield Observed in Magnetized Indirectly Driven D 2 -Filled Capsule Implosions on the National Ignition Facility. *Physical Review Letters*, 129(19):195002, November 2022. ISSN 0031-9007, 1079-7114. doi: 10.1103/PhysRevLett.129.195002. URL <https://link.aps.org/doi/10.1103/PhysRevLett.129.195002>. 7
- [3] A. Bose, J. Peebles, C. A. Walsh, J. A. Frenje, N. V. Kabadi, P. J. Adrian, G. D. Sutcliffe, M. Gatu Johnson, C. A. Frank, J. R. Davies, R. Betti, V. Yu. Glebov, F. J. Marshall, S. P. Regan, C. Stoeckl, E. M. Campbell, H. Sio, J. Moody, A. Crilly, B. D. Appelbe, J. P. Chittenden, S. Atzeni, F. Barbato, A. Forte, C. K. Li, F. H. Seguin, and R. D. Petrasso. Effect of Strongly Magnetized Electrons and Ions on Heat Flow and Symmetry of Inertial Fusion Implosions. *Physical Review Letters*, 128(19):195002, May 2022. ISSN 0031-9007, 1079-7114. doi: 10.1103/PhysRevLett.128.195002. URL <https://link.aps.org/doi/10.1103/PhysRevLett.128.195002>. 7
- [4] A. Colaïtis, I. Igumenshchev, J. Mathiaud, and V. Goncharov. Inverse ray tracing on icosahedral tetrahedron grids for non-linear laser plasma interaction coupled to 3D radiation hydrodynamics. *Journal of Computational Physics*, 443:110537, October 2021. ISSN 0021-9991. doi: 10.1016/j.jcp.2021.110537. URL <https://www.sciencedirect.com/science/article/pii/S0021999121004320>. 12

Permissions